Growth and characterization of pyrochlore-type $(Ca,Ti)_2(Nb,Ti)_2O_7$ thin films

Jing-Wei Yin[a], Yan Wang[a], Yue-Hua Chen[b], Sheng-Qiang Wu[a], Shao-Dong Cheng[a], Shao-Bo Mi[a,*], Lu Lu[a], Lei Jin[c,*], Hong Wang[a,d]

[a]*State Key Laboratory for Mechanical Behavior of Materials & School of Microelectronics, Xi'an Jiaotong University, Xi'an 710049, China*

[b]*Key Laboratory for Organic Electronics and Information Displays & Institute of Advanced Materials, Nanjing University of Posts & Telecommunications, Nanjing 210023, China*

[c]*Ernst Ruska-Centre for Microscopy and Spectroscopy with Electrons, Forschungszentrum Jülich GmbH, 52425 Jülich, Germany*

[d]*Department of Materials Science and Engineering, Southern University of Science and Technology, Shen Zhen 518055, China*

Abstract

Pyrochlore-type $(Ca,Ti)_2(Nb,Ti)_2O_7$ thin films have been grown on single-crystalline $LaAlO_3$ and yttria-stabilized zirconia substrates by a magnetron sputtering system. Atomic-scale interface structure and growth mode of the $(Ca,Ti)_2(Nb,Ti)_2O_7$ films on the substrates with different crystal structures have been investigated by advanced electron microscopy techniques. In both heterosystems, the film/substrate orientation relationship of $[100](001)_{film}//[100](001)_{substrate}$ has been

∗ E-mail: shaobo.mi@xjtu.edu.cn; l.jin@fz-juelich.de
Fax: +86 (29) 83395679
Tel: +86 (29) 83395023

determined. In the heterosystem of $(Ca,Ti)_2(Nb,Ti)_2O_7$/yttria-stabilized zirconia, the films directly grow on the substrates. In contrast, in the $(Ca,Ti)_2(Nb,Ti)_2O_7/LaAlO_3$ heterosystem, a perovskite-type $Ca_{1-□}(Ti,Nb)O_3$ interlayer with a few unit cells in thickness forms at the interface and interfacial reconstruction occurs at the $(Ca,Ti)_2(Nb,Ti)_2O_7/Ca_{1-□}(Ti,Nb)O_3$ interface. Our findings indicate that the formation of the interlayer and the $(Ca,Ti)_2(Nb,Ti)_2O_7/Ca_{1-□}(Ti,Nb)O_3$ interface reconstruction can accommodate the film/substrate dissimilarities in the crystal structures and facilitate the growth of single-crystalline pyrochlore-type films on the perovskite-type substrates.

Keywords: Thin Films; Interfaces; Pyrochlore-type Structure; Film Growth, Advanced Electron Microscopy

1. Introduction

Pyrochlore structured $A_2B_2O_7$ oxides with high dielectric permittivity, low dielectric loss, and high dielectric tunability have been considered as promising candidates for application in tunable microwave devices (e.g., phase shifters, capacitors, and coplanar waveguides) [1-3]. In particular, the aliovalent cations can be incorporated on A or B lattice sites or both, which results in unusual properties (e.g., dielectric relaxation behavior) in the compounds [4-6]. Compared with the bulk counterpart, pyrochlore-type materials in thin-film form are desired for various device applications. Also, the epitaxial pyrochlore-type films are expected to have superior properties to the polycrystalline films. Consequently, it is important to choose suitable substrates for the growth of pyrochlore-type films having high quality and

performance. The single crystalline perovskite crystals (e.g., $SrTiO_3$ and $LaAlO_3$) with the low dielectric loss are suitable substrates for the growth of pyrochlore films [7, 8]. Additionally, considering functional films (e.g. superconducting $YBa_2Cu_3O_{7-\delta}$ [9] and ferroelectric $Pb(Zr,Ti)O_3$ [10]) frequently prepared on perovskite-type substrates, it is important to understand the structural properties of the pyrochlore/perovskite heterosystems for having functional diversity in the composite films. However, it seems difficult to fabricate the epitaxial pyrochlore-type films on perovskite-type substrates due to the dissimilarities in the crystal structures and the large lattice mismatch between films and substrates [7, 8]. Moreover, the detailed interface properties and the film growth behavior remain unclear in the heterostructures of the pyrochlore-type film prepared on the substrate with different crystal structures [11, 12].

In this work, the single-crystalline pyrochlore-type $(Ca,Ti)_2(Nb,Ti)_2O_7$ (CNTO) films have been fabricated on perovskite-type $LaAlO_3$ (LAO) substrates and fluorite-type yttria-stabilized zirconia (YSZ), respectively. Our research interests mainly focus on atomic-scale understanding of the growth mode of the CNTO films and the interface structure by using advanced electron microscopy techniques.

2. Materials and methods

In the Ca–Ti–Nb–O system, a pyrochlore-type phase forms at $Ca_{1.46}Nb_{1.11}Ti_{1.38}O_7$, which has low levels of vacancies on A or oxygen lattice sites or both in the pyrochlore-type structure [13]. In this work, the ceramic target with a nominal composition of $Ca_{1.46}Nb_{1.11}Ti_{1.38}O_7$ was prepared by using conventional solid-state reaction route with high-purity oxides ($CaCO_3$, TiO_2 and Nb_2O_5) in a stoichiometric ratio [14]. The CNTO films were fabricated on (001)-oriented YSZ and LAO

substrates by magnetron sputtering deposition under the oxygen flowing pressure of 2.5×10^2 Pa and at a substrate temperature of 850 °C. The substrate temperature was measured by employing a very thin thermocouple placed in a hole at the side of the dummy substrate just lying on the heater. During sputtering the target-substrate distance of 2 cm, and current density of 15 mA/cm^2 have been used for the fabrication of CNTO films. After the film deposition, the cooling rate of the samples was 5 °C/min from 850 °C to room temperature in pure O_2 under 5×10^4 Pa.

The crystallinity of the CNTO films prepared on different substrates was analyzed by high-resolution X-ray diffraction using a PANalytical X'Pert MRD. Diffraction data were acquired by exposing the samples to Cu-Kα X-ray radiation and the X-ray source was operated at 40 mA filament current and 40 kV acceleration voltage. Cross-sectional transmission electron microscopy (TEM) and scanning TEM (STEM) specimens were prepared by focused ion beam technique (FEI Helios Nanolab 600i) [15]. Selected-area electron diffraction (SAED), diffraction-contrast imaging, high-angle annular dark-field (HAADF) imaging, and energy-dispersive X-ray spectroscopy (EDS) mapping were performed on a JEOL ARM200F microscope equipped with a probe aberration corrector and an Oxford X-Max^N 100TLE spectrometer, operated at 200 kV.

3. Results and discussion

Fig. 1a displays a typical XRD θ-2θ scan of the as-grown CNTO film prepared on the LAO substrate at 850 ℃. To simplify the following discussion, rhombohedrally distorted LAO (PDF 31-0022) is treated as a pseudocubic structure with a lattice parameter of $a_{\mathrm{LAO}pc}$ = 0.379 nm [16]. In Fig. 1a, apart from the peaks of the substrate, additional peaks related to the film appear, and can be indexed as the $(00l)_{\mathrm{CNTO}}$ planes

(as marked by asterisks) by comparing with the Powder Diffraction File (PDF) of $Ca_{1.5}NbTi_{1.5}O_7$ (PDF 30-0270). The out-of-plane lattice parameter of the CNTO film is calculated to be 1.027(4) nm, which is slightly larger than that of the bulk CNTO (a_{CNTO} = 1.023 nm) [13, 14]. Fig. 1b shows a low-magnification bright-field (BF) TEM image of the CNTO/LAO$(001)_{pc}$ heterostructure. The thickness of CNTO film is about 18 nm and no contrast variation related to the formation of misfit dislocations are observed at the interface. The chemical composition of the CNTO film is measured by EDS. Compared with the cation ratio (1.46Ca:1.11Nb:1.38Ti) of the ceramic target, the cation composition ratio (1.38 ± 0.05Ca:1.23 ± 0.04Nb:1.41 ± 0.05Ti) of the film is slightly different, which may result from the volatilization of Ca and Ti elements during thin-film deposition. The SAED pattern of the CNTO/LAO heterostructure viewed along the LAO$[100]_{pc}$ zone axis is inserted in Fig. 1b. The diffraction spots from CNTO and LAO can be distinguished, as marked by a red and a white open square, respectively. Using the diffraction spots of LAO as the calibration standard (e.g. $001_{LAO pc}$), the spacing of crystallographic planes of CNTO can be calculated, and the diffraction spots of CNTO can be indexed, as demonstrated by a red arrow. Accordingly, the film/substrate crystallographic OR of $[100](001)_{CNTO}//[100]_{pc}(001)_{pc\text{-}LAO}$ can be obtained.

Fig. 2a displays an atomic-scale HAADF-STEM image of the CNTO/LAO heterointerface viewed along the LAO$[100]_{pc}$ zone axis, showing the formation of a thin interlayer between CNTO and LAO, as denoted by horizontal arrows. It can be seen that the interlayer coherently grows on the LAO substrate with a few unit cells in thickness. The chemical composition of the interlayer-layer has been characterized by atomic-resolution EDS elemental mapping [17]. Figs. 2b–f show a high-resolution HAADF image and the corresponding EDS maps of Al, La, Ca, Ti, and Nb of the

interlayer/LAO interface. In the interlayer layer, Ti and Nb cations locate in the same atomic columns (Figs. 2f and 2g). The Ca cations site in the center of four adjacent Ti/Nb cations (Fig. 2e), indicating that the interlayer possesses a perovskite-type ABO_3 structure. In fact, the intensity variation of Ca columns can be visible in Fig. 2a, as demonstrated by a pair of vertical green arrows, which could result from the Ca vacancy in the columns. The appearance of Ca vacancies can maintain the neutrality of the interlayer. Accordingly, the chemical formula of $Ca_{1-□}(Ti,Nb)O_3$ is applied to the interlayer. The coherent growth of the pseudocubic $Ca_{1-□}(Ti,Nb)O_3$ interlayer on LAO results in an identical in-plane lattice parameter (0.379 nm) between the interlayer and the substrate. The out-of-plane lattice parameter of the interlayer measured in Fig. 2a is 0.391±0.003 nm by using the lattice parameter of the substrate (0.379 nm) as a reference. It should be noted that in Fig. 1a the diffraction peaks of the interlayer may have quite low intensity, which cannot be detected in the XRD diffraction pattern.

At the CNTO/$Ca_{1-□}(Ti,Nb)O_3$ interface, every three (004) planes of the pyrochlore-type film match two $(001)_{pc}$ planes of the perovskite-type interlayer. Accordingly, a 3-to-2 coincidence site lattice (CSL) model can be applied to describe the epitaxial relationship between CNTO and $Ca_{1-□}(Ti,Nb)O_3$ [18], and a corresponding coincidence misfit of F_0 = -1.20% can be obtained, indicating that the CNTO film grown on $Ca_{1-□}(Ti,Nb)O_3$ undertakes in-plane biaxial compressive strain. No misfit dislocations appear at the interface, indicating that the epitaxial strain of the film system may be accommodated by the elastic deformation of the lattice.

Fig. 3a shows a magnified HAADF-STEM image of the CNTO/$Ca_{1-\square}(Ti,Nb)O_3$ interface viewed along the LAO$[100]_{pc}$ zone axis, which indicates that the interlayer terminates at the $(Ti,Nb)O_2$ atomic plane at the interface. Based on the experimental observation, Fig. 3b illustrates a structure model of the CNTO/$Ca_{1-\square}(Ti,Nb)O_3$ interface projected along the $[100]_{CNTO}$ zone axis. In Fig. 3a, both interfacial $(Ti,Nb)O_2$ and CaO planes (denoted by a horizontal purple and a horizontal cyan arrows, respectively) have relatively low intensity compared with other $(Ti,Nb)O_2$ and CaO planes in the $Ca_{1-\square}(Ti,Nb)O_3$ layer. Fig. 3c displays the change of intensity for the atomic columns along the red broken-line in Fig. 3a. It can be seen that in Fig. 3c the intensity of the interfacial Ti/Nb–O column (indicated by a vertical purple arrow) and the cation column in the CNTO (marked by a vertical red arrow) is comparable, but much lower than that of other Ti/Nb–O columns (illustrated by vertical black arrows) in $Ca_{1-\square}(Ti,Nb)O_3$. It is known that under the HAADF-STEM imaging conditions, the intensity of the cation column is approximately proportional to Z^2 (Z is the atomic number averaged in the atomic columns) [19, 20]. Therefore, the low intensity of the interfacial planes indicates that a high density of cation deficiency may appear in the interfacial $(Ti,Nb)O_2$ and CaO planes.

To further understand these phenomena, the interface structure has been studied along the LAO$[1\bar{1}0]_{pc}$ zone axis by atomic-resolution HAADF-STEM imaging. Fig. 4a shows a typical HAADF-STEM image of the CNTO/$Ca_{1-\square}(Ti,Nb)O_3$ interface. In Fig. 4a the intensity variation of cation columns appears at the interfacial $(Ti,Nb)O_2$ and (Ca,Ti)/(Nb,Ti) planes periodically, as indicated by vertical arrows. Assuming that

the interfacial $Ca_{1-\square}(Ti,Nb)O_3$ and CNTO planes are complete, an unrelaxed CNTO/$Ca_{1-\square}(Ti,Nb)O_3$ interface structure model viewed along the $[1\bar{1}0]_{CNTO}$ zone axis can be built, as shown in Fig. 4b. It should be noted that no intensity variations of cation columns would occur at interfacial $(Ti,Nb)O_2$ (indicated by a horizontal purple arrow) plane and (Ca,Ti)/(Nb,Ti) plane (indicated by a horizontal red arrow) in the unrelaxed interface structure model. A top-view and the corresponding side-view of the unrelaxed interface is shown in Fig. 4c, which contains only cations in the interfacial $(Ti,Nb)O_2$ and (Ca,Ti)/(Nb,Ti) planes. Across the unrelaxed CNTO/$Ca_{1-\square}(Ti,Nb)O_3$ interface, the distance between neighboring cations can be determined to be about 0.14, 0.23, 0.29, and 0.39 nm, respectively, as indicated in the top-view of the interface model. In fact, the distance of 0.14 and 0.23 nm between neighboring cations across the interface is much shorter than the shortest distance of neighboring cations in CNTO and $Ca_{1-\square}(Ti,Nb)O_3$ (~0.36 nm in CNTO and ~0.33 nm in $Ca_{1-\square}(Ti,Nb)O_3$, respectively). Based on the experimental observation (Fig. 4a), it can be concluded that the reconstruction mainly occurs for the interfacial cations with shorter distances across the interface. Fig. 4d shows a proposed top-view and side-view of the relaxed structure model of the CNTO/$Ca_{1-\square}(Ti,Nb)O_3$ interface that only contains cations in the interfacial planes. For the interfacial cations with a distance of ~0.14 nm in Fig. 4c, cation vacancies mainly appear at the interfacial $(Ti,Nb)O_2$ plane in the relaxed structure model. In contrast, cation vacancies mainly appear at interfacial (Ca,Ti)/(Nb,Ti) plane for the interfacial cations with a distance of ~0.23 nm in Fig. 4c. Compared with the unrelaxed structure model in Fig. 4c, the density of cations

becomes low for the sites marked by broken-line ellipses in the side-view of the relaxed structure model in Fig. 4d. Accordingly, the low intensity of these cation columns would appear in the HAADF image displayed in Fig. 4a. The purple and the yellow arrows indicate the cation columns that are not affected by the cation reconstruction in the interfacial (Ca,Ti)(Nb,Ti) and $(Ti,Nb)O_2$ planes, respectively, which has a good match well with the experimental results displayed in Fig. 4a. It should be mentioned that to keep the interface neutrality more A-site cation vacancies occur in the interfacial CaO plane, which results in the CaO atomic plane (denoted by a horizontal green arrow in Fig. 4a) having a relatively low intensity compared with other CaO planes in the $Ca_{1-\square}(Ti,Nb)O_3$ layer.

To understand the growth behavior of the pyrochlore-type film on the substrate with different crystal structures, the CNTO films have been prepared on fluorite-type YSZ substrates. A typical XRD pattern of the as-grown CNTO film on the YSZ substrate is shown in Fig. 5a. Indexing of the peaks of the substrate and the film appear indicates that a (00l)-oriented CNTO thin film has been obtained. The calculated out-of-plane lattice parameter of the CNTO film on YSZ is 1.022(5) nm, which is slightly smaller than that of the film on LAO. Fig. 5b displays a low-magnification BF-TEM image of the CNTO/YSZ(001) heterostructure. The CNTO film is about 20 nm in thickness and no misfit dislocations are observed at the interface. The SAED pattern of the heterostructure recorded along the YSZ[100] zone axis is displayed in Fig. 5c. The small lattice mismatch ($\frac{2\times d_{YSZ}-d_{CNTO}}{2\times d_{YSZ}} \approx 0.4\%$) results in that the diffractions of YSZ substrate cannot be separated from those of CNTO film, e.g., $0\overline{44}_{YSZ}$ and $0\overline{22}_{CNTO}$ denoted by a vertical white arrow. Nevertheless, the structure difference between YSZ and CNTO leads to the appearance of weak

diffraction spots from the pyrochlore-type CNTO film in the SAED pattern, as demonstrated by a vertical red arrow. The crystallographic orientation relationship (OR) of $[100](001)_{CNTO}//[100](001)_{YSZ}$ between CNTO and YSZ can be concluded. Fig. 5d is a typical high-resolution HAADF-STEM image of the CNTO/YSZ heterostructure viewed along the YSZ[100] zone axis, showing the coherent growth of the CNTO film on the YSZ substrate. The misfit strain between the 20-nm-thick CNTO film and YSZ substrate can be accommodated by the elastic deformation of the crystal lattice.

The difference between the fluorite- and pyrochlore-type structures can be easily distinguished along the ⟨110⟩ zone axis, as illustrated in the structure mode in Fig, 6a. A typical high-resolution HAADF-STEM image of the CNTO/YSZ heterostructure viewed along the YSZ[$1\bar{1}0$] zone axis is shown in Fig. 6b. The intensity variation of atomic planes can be visible in the CNTO film, as demonstrated by a horizontal red arrow. The corresponding SAED pattern of the CNTO/YSZ heterostructure is inserted in Fig. 6b. Apart from the diffraction spots of YSZ, weak diffraction spots from the CNTO film can be indexed as a pyrochlore-type structure. In other words, the CNTO film with a pyrochlore-type structure on the fluorite-type YSZ substrate can be concluded from both HAADF-STEM and SAED experiments.

Figs. 6c-f show a high-resolution HAADF image and the corresponding EDS maps of Ca, Ti, and Nb of the CNTO film. Ti and Nb cations locate in the same atomic columns (Figs. 6e and 6f), which display the highest intensity in the HAADF image, as indicated by a white arrow in Fig. 6c. The EDS maps in Figs. 6d-f indicate the coexistence of Ca, Ti, and Nb cations in the same columns, which agrees with the structure model displayed in Fig. 6a. The cation sites containing Ca, Ti, and Nb are

demonstrated by a red arrow in Fig. 6c. Additionally, according to the structure model in Fig. 6a, the Ca and Ti cations site in the position indicated by a blue arrow in Fig. 6c. But, due to the partial occupancy of Ti cations in the CNTO lattice (Site 96g) [13], only Ca cations (Fig. 6d) can be detected under our experimental conditions.

The slight difference in crystallographic structure between the fluorite and pyrochlore structures may facilitate the growth of the pyrochlore-type CNTO films on the YSZ substrates directly. In contrast, the interfacial cation reconstruction may not easily occur for the CNTO film prepared at the as-received LAO substrate under our experimental conditions. Without the cation reconstruction, the atomic density at the CNTO/LAO interface is the same as that at the unrelaxed CNTO/$Ca_{1-\square}(Ti,Nb)O_3$ interface mode in Fig. 4c, which makes difficulty in growing the pyrochlore-type films on LAO substrates directly. Experimental evidence indicates that the perovskite-type LAO substrate favors the growth of a few-unit-cell-thick perovskite-type interlayer on the perovskite-type LAO substrates firstly before the pyrochlore-type films. Then, in the course of film deposition, the change of local composition of the interlayer occurs, which is fit for the growth conditions of the pyrochlore-type CNTO films. Accordingly, a reconstructed interface appears between the pyrochlore- and perovskite-type structures.

Additionally, for the epitaxial growth of high-quality films, the lattice mismatch between films and substrates is a critical parameter [16, 21-24]. Table I lists the crystal structure and lattice parameters of bulk CNTO, LAO, $NdGaO_3$ [25], $SrTiO_3$ [26], and YSZ [27]. In addition, lattice mismatch (or coincidence misfit) in the heterosystems has been calculated by using the formula of $(m*a_s-n*a_f)/m*a_s$, where m and n are positive integers; a_s and a_f represent the lattice spacing of the substrate and

the film in the CSL model [18]. It is noted that compared with the CNTO/LAO system, the film undertakes tensile strain in the CSL model for the CNTO/$SrTiO_3$ and CNTO/$NdGaO_3$ system. A relatively large tensile strain may result in the formation of the polycrystalline CNTO film with nano-columnar structure on the $SrTiO_3$ substrates [20]. From this viewpoint, the compressive strain in the CSL model favors the growth of the single-crystalline pyrochlore-type CNTO film on the LAO substrate. It is known that the epitaxial strain affects not only the growth mode of thin film but also the formation of planar defects in the heterosystems [28, 29]. The formation of planar defects (e.g. twins) within the polycrystalline CNTO film may relax the growth strain in the film system. In comparison, nanosized twin domains do not form within the single-crystalline pyrochlore-type CNTO films on both LAO and YSZ.

4. Conclusion

Single-crystalline pyrochlore-type CNTO thin films have been prepared on perovskite-type $LaAlO_3$ and fluorite-type YSZ substrates, respectively. A film/substrate cube-on-cube OR occurs in both heterosystems. In contrast to the direct growth of the CNTO films on the YSZ substrates, the formation of a thin perovskite-type $Ca_{1-\square}(Ti,Nb)O_3$ intermediate layer with the reconstruction at the CNTO/$Ca_{1-\square}(Ti,Nb)O_3$ interface enables the epitaxial growth of the CNTO films on the $LaAlO_3$ substrates. The findings in the CNTO/$LaAlO_3$ heterosystem can be helpful to understand the growth behavior of the pyrochlore-type films on the perovskite-type substrates in other heterosystems.

Acknowledgements

The work was supported by the National Natural Science Foundation of China (Nos.

51471169, 51901172 and 2017YFB0406303) and the National Basic Research Program of China (No. 2015CB654903).

References

[1] M.A. Subramanian, G. Aravamudan, G.V.S. Rao, Oxide pyrochlores - a review, Prog. Solid State Chem. 15 (1983) 55–143.

[2] T.A. Vanderah, I. Levin, M.W. Lufaso, An unexpected crystal- chemical principle for the pyrochlore structure, Eur. J. Inorg. Chem. 2005 (2010) 2895–2901.

[3] R.J. Cava, W.F. Peck, J.J. Krajewski, Pyrochlore based oxides with high dielectric constant and low temperature coefficient, J. Appl. Phys. 78 (1995) 7231–7233.

[4] S. Kamba, V. Porokhonskyy, A. Pashkin, V. Bovtun, J. Petzelt, J.C. Nino, S. Troliermckinstry, M.T. Lanagan, C.A. Randall, Anomalous broad dielectric relaxation in $Bi_{1.5}Zn_{1.0}Nb_{1.5}O_7$ pyrochlore, Phys. Rev. B 66 (2002) 054106.

[4] V. Krayzman, I. Levin, J. C. Woicik, Local Structure of Displacively Disordered Pyrochlore Dielectrics, Chem. Mater. 19 (2007) 932–936

[6] N. Binh, Y. Liu, R.L. Withers, Relaxor dielectric properties of a $(Ca_{1.5}Ti_{0.5})(NbTi)O_7$ 'misplaced-displacive' cubic pyrochlore synthesised via metallorganic decomposition. Solid State Commun. 145 (2008) 72–76.

[7] C. Jiménez, T. Caroff, L. Rapenne, S. Morlens, E. Santos, P. Odier, F. Weiss, Effect of the annealing process on the microstruture of $La_2Zr_2O_7$ thin layers epitaxially grown on $LaAlO_3$ by metalorganic decomposition, J. Cryst. Growth 311 (2009) 3204–3210.

[8] S. Saitzek, Z. Shao, A. Bayart, A. Ferri, M. Huve, P. Roussel, R. Desfeux, Ferroelectricity in $La_2Zr_2O_7$ thin films with a frustrated pyrochlore-type structure, J. Mater. Chem. C 2 (2014) 4037–4043.

[9] S.-B. Mi, T. Yao, S.-D. Cheng, M.I. Faley, U. Poppe, L. Lu, D. Wang, C.-L. Jia,

Atomic-scale imaging of interfacial polarization in cuprate-titanate heterostructures, Appl. Phys. Lett. 116 (2020) 251603.

[10] S. B. Mi, C. L. Jia, L. Vrejoiu, M. Alexe, D. Hesse, Atomic-Scale Structure and Properties of Epitaxial $PbZr_{0.2}Ti_{0.8}O_3/SrRuO_3$ Heterointerfaces, Adv. Mater. Interfaces, 2 (2015) 1500087.

[11] J. Cagnon, D.S. Boesch, N.H. Finstrom, S.Z. Nergiz, S.P. Keane, S. Stemmer, Microstructure and dielectric properties of pyrochlore $Bi_2Ti_2O_7$ thin films, J. Appl. Phys. 102 (2007) 044102.

[12] D.P. Norton, Synthesis and properties of epitaxial electronic oxide thin-film materials, Mater. Sci. Eng. R 43 (2004) 139–247.

[13] R.S. Roth, T.A. Vanderah, P. Bordet, I.E. Grey, W.G. Mumme, L. Cai, J.C. Nino, Pyrochlore formation, phase relations, and properties in the $CaO–TiO_2–(Nb,Ta)_2O_5$ Systems, J. Solid State Chem. 181 (2008) 406–414.

[14] Y. Chen, Phase Structure and Dielectric Properties of New Pyrochlore Dielectric Ceramics, Ph.D thesis, Xi'an Jiaotong University, 2014.

[15] K. Liu, R. Zhang, L. Lu, S.-B. Mi, M. Liu, H. Wang, S. Wu, C.-L. Jia, Atomic-scale investigation of spinel $LiFe_5O_8$ thin films on $SrTiO_3$(001) substrates, J. Mater. Sci. Technol. 40 (2020) 31–38.

[16] S. Wu, S. Cheng, L. Lu, M. Liu, X.-W. Jin, S.-D. Cheng, S.-B. Mi, B-site ordering and strain-induced phase transition in double-perovskite La_2NiMnO_6 films, Sci. Reports 8 (2018) 2516.

[17] P. Lu, L. Zhou, M. J. Kramer, D. J. Smith, Atomic-scale chemical imaging and quantification of metallic alloy structures by energy-dispersive X-ray spectroscopy, Sci. Reports 4 (2014) 3945.

[18] A. Trampert, K.H. Ploog, Heteroepitaxy of large-misfit systems: role of

coincidence lattice, Cryst. Res. Technol. 35 (2000) 793–806.

[19] S. Yamashita, J. Kikkawa, K. Yanagisawa, T. Nagai, K. Ishizuka, K. Kimoto, Atomic number dependence of Z contrast in scanning transmission electron microscopy, Sci. Reports 8 (2018) 12325.

[20] P. D. Nellist, S. J.Pennycookm, The principles and interpretation of annular dark-field Z-contrast imaging, Adv. Imag. Electron. Phys. 113 (2000) 147–203.

[21] S.Q. Wu, Y.H. Chen, Y. Wang, H. Wang, K. Liu, S.B. Mi, Interface structure and planar defects in the heterostructure of pyrochlore-type $(Ca,Ti)_2(Nb,Ti)_2O_7$ film on $SrTiO_3$ (001) substrate, J. Cryst. Growth 519 (2019) 20–24.

[22] J. Lu, D.O. Klenov, S. Stemmer, Influence of strain on the dielectric relaxation of pyrochlore bismuth zinc niobate thin films, Appl. Phys. Lett., 84 (2004) 957.

[23] T. L. Meyer, L. Jiang, S. Park, T. Egami, and H. N. Lee, Strain-relaxation and critical thickness of epitaxial $La_{1.85}Sr_{0.15}CuO_4$ films, Apl. Mater. 3 (2015)126102.

[24] C.-M. Wang, S. Thevuthasan, C. H. F. Peden, Interface Structure of an Epitaxial Cubic Ceria Film on Cubic Zirconia, J. Am. Ceram. Soc. 86 (2003) 363–65.

[25] A. Marezio, J.P. Remeika, P.D. Dernierr, Rare earth orthogallates, Inorg. Chem. **7** (1968) 1337–1340.

[26] S.A. Howard, J.K. Yau, H.U. Anderson, Structural characteristics of $Sr_{1-x}La_xTiO_{3\pm\delta}$ as a function of oxygen partial-pressure at 1400 ℃, J. Appl. Phys. 65 (1989) 1492–1498.

[27] http://www.crystec.de/daten/ysz.pdf

[28] K. Liu, R. Zhang, L. Lu, S.-B. Mi, M. Liu, H. Wang, S. Wu, C. Jia. Atomic-scale investigation of spinel $LiFe_5O_8$ thin films on $SrTiO_3$(001) substrates. J. Mater. Sci. Technol. 40 (2020) 31–38,

[29] S.-B. Mi, R. Zhang, L. Lu, M. Liu, H. Wang, C.-L. Jia. Atomic-scale structure and formation of antiphase boundaries in α-$Li_{0.5}Fe_{2.5}O_4$ thin films on $MgAl_2O_4$(001) substrates, Acta Mater. 127 (2017) 178–184.

Figure Captions

Fig.1. (a) A typical XRD θ-2θ scan of the as-grown CNTO film prepared on the LAO substrate. The $(00l)_{CNTO}$ peaks of the film are marked by asterisks. (b) A low-magnification BF-TEM image showing an overview of the CNTO/LAO heterostructure. The interface is indicated by a horizontal yellow arrow. The insert is the SAED pattern of the heterostructure recorded along the LAO$[100]_{pc}$ zone axis.

Fig. 2. (a) A high-resolution HAADF-STEM image showing the structure details at the CNTO/LAO interface, viewed along the LAO$[100]_{pc}$ zone axis. A pair of vertical green arrows demonstrate the intensity variation in the Ca columns. (b-g) A HAADF-STEM image and the corresponding EDS maps showing the distribution of Al, La, Ca, Ti, and Nb at the heterointerface. The interface of LAO/interlayer is indicated by a horizontal yellow arrow, and CNTO/interlayer by a horizontal red arrow.

Fig. 3. (a) and (b) An atomic-resolution HAADF-STEM image and an unrelaxed structure model of the CNTO/$Ca_{1-□}(Ti,Nb)O_3$ interface, viewed along the LAO$[100]_{pc}$ zone axis. The interfacial CaO, $(Ti,Nb)O_2$, and (Ca,Ti)/(Nb,Ti) plane is denoted by a horizontal green, purple and red arrow, respectively. (c) The intensity line profiles for cation columns indicated by a red broken-line in (a). Interfacial Ti/Nb–O and (Ca,Ti)/(Nb,Ti) column is indicated by a purple and a red arrow, respectively. Ti/Nb–O columns with different intensity from the interfacial Ti/Nb–O column are

denoted by vertical black arrows.

Fig. 4. (a) and (b) A typical HAADF-STEM image and an unrelaxed structure model of the CNTO/$Ca_{1-\square}(Ti,Nb)O_3$ interface, viewed along the LAO$[1\bar{1}0]_{pc}$ zone axis. The interfacial CaO, $(Ti,Nb)O_2$, and (Ca,Ti)/(Nb,Ti) plane is denoted by a horizontal green, purple and red arrow, respectively. The vertical arrows indicate the intensity variation at the $(Ti,Nb)O_2$ and (Ca,Ti)/(Nb,Ti) planes. (c) and (d) The top-view and the side-view of the unrelaxed and the relaxed CNTO/$Ca_{1-\square}(Ti,Nb)O_3$ interface model. In (d), the low-density cation columns are marked by broken-line ellipses in the side-view of the relaxed structure model. Purple arrows and yellow arrows in (d) indicate the cation columns without the reconstruction at the (Ca,Ti)/(Nb,Ti) and $(Ti,Nb)O_2$ planes, respectively.

Fig. 5. (a) A typical XRD θ-2θ scan of the as-grown CNTO film prepared on the YSZ substrate. The $(00l)_{CNTO}$ peaks of the film are marked by asterisks. (b) A low-magnification BF-TEM image of the CNTO/LAO heterostructure showing the coherent growth of 20-nm-thick CNTO film on YSZ substrate. (c) The SAED pattern of the heterostructure recorded along the YSZ[100] zone axis. (d) A high-resolution HAADF-STEM image of the CNTO/YSZ heterostructure. The film-substrate interface is denoted by a horizontal white arrow.

Fig. 6. (a) A structure model of the CNTO and YSZ projected along the $[1\bar{1}0]$ crystallographic direction. (b) A high-resolution HAADF-STEM image of the CNTO/YSZ heterostructure recorded along the YSZ[100] zone axis. The intensity variation within the film is indicated by a horizontal red arrow. The interface is indicated by a horizontal white arrow. The insert is the corresponding SAED pattern

of the heterostructure. (c) A high-resolution HAADF-STEM image and the corresponding EDS maps of Ca, Ti, and Nb of the film showing the cation distribution in the CNTO lattice.

Table 1. The crystal structure and lattice parameters of bulk CNTO, $LaAlO_3$, $NdGaO_3$, $SrTiO_3$, and YSZ are listed. Lattice mismatch (or coincidence misfit) (F_0) is calculated using the formula of $F_0 = (m*a_s-n*a_f)/m*a_s$.

Table 1

Material	Crystallographic Structure	Unit cell lattice parameters (nm)						In-plane direction	Lattice mismatch (or coincidence misfit)
		a	b	c	a_{pc}	b_{pc}	c_{pc}		
CNTO	Cubic ($Fd\bar{3}m$)	1.023	1.023	1.023	-	-	-	[100]	-
$LaAlO_3$	Rhombohedral ($R\bar{3}c$)	0.5365	0.5365	1.3111	0.379	0.379	0.379	$[100]_{pc}$	-1.20%
$NdGaO_3$	orthorhombic ($Pbnm$)	0.5431	0.5499	0.7710	0.386	0.386	0.386	$[100]_{pc}$	0.62%
$SrTiO_3$	Cubic ($Pm\bar{3}m$)	0.3905	0.3905	0.3905	-	-	-	[100]	1.76%
YSZ	Cubic ($Fm\bar{3}m$)	0.512	0.512	0.512	-	-	-	[100]	0.4%

FIG 1

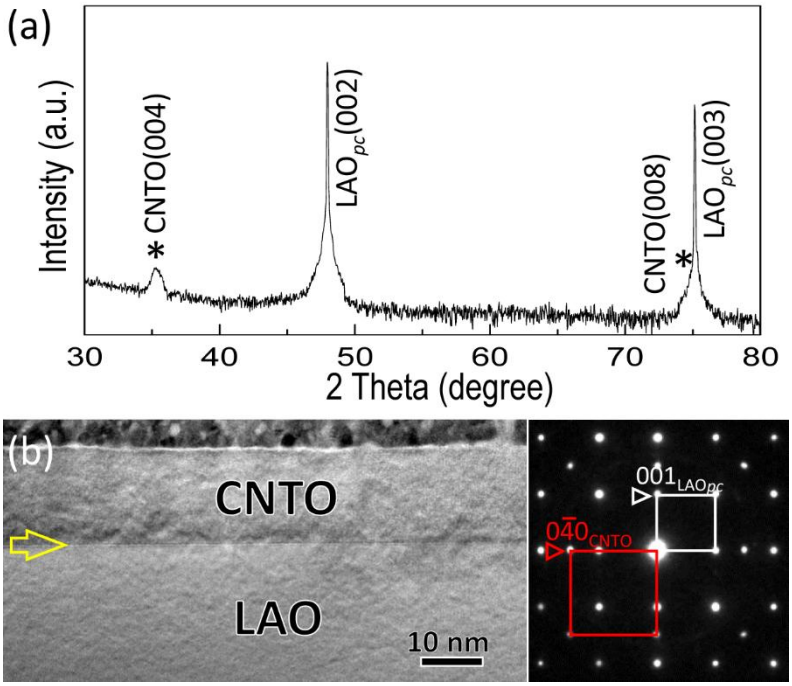
(a)
Intensity (a.u.)
* CNTO(004)
LAO$_{pc}$(002)
CNTO(008)
*
LAO$_{pc}$(003)
30
40
50
60
70
80
2 Theta (degree)
(b)
CNTO
LAO
10 nm
001$_{LAO_{pc}}$
$0\bar{4}0_{CNTO}$

FIG 2

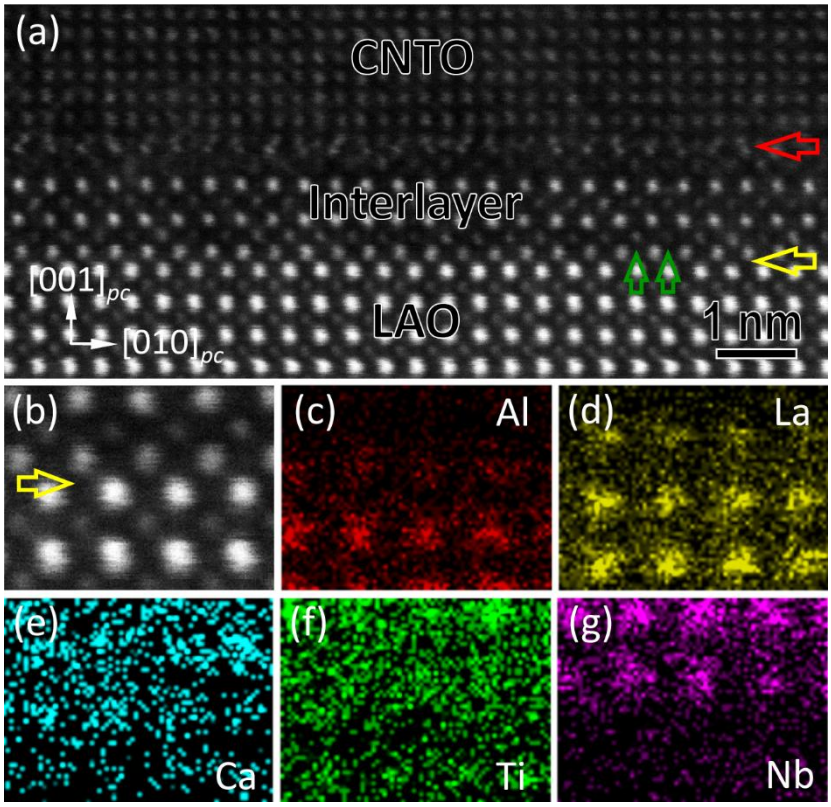

FIG 3

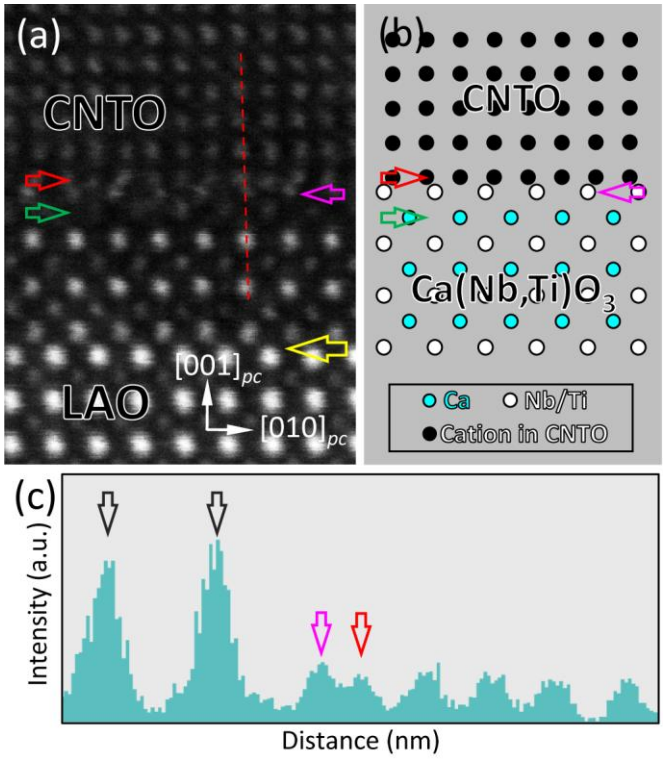
(a)
CNTO
LAO
[001]pc
[010]pc
(b)
CNTO
Ca(Nb,Ti)O3
Ca
Nb/Ti
Cation in CNTO
(c)
Intensity (a.u.)
Distance (nm)

FIG 4

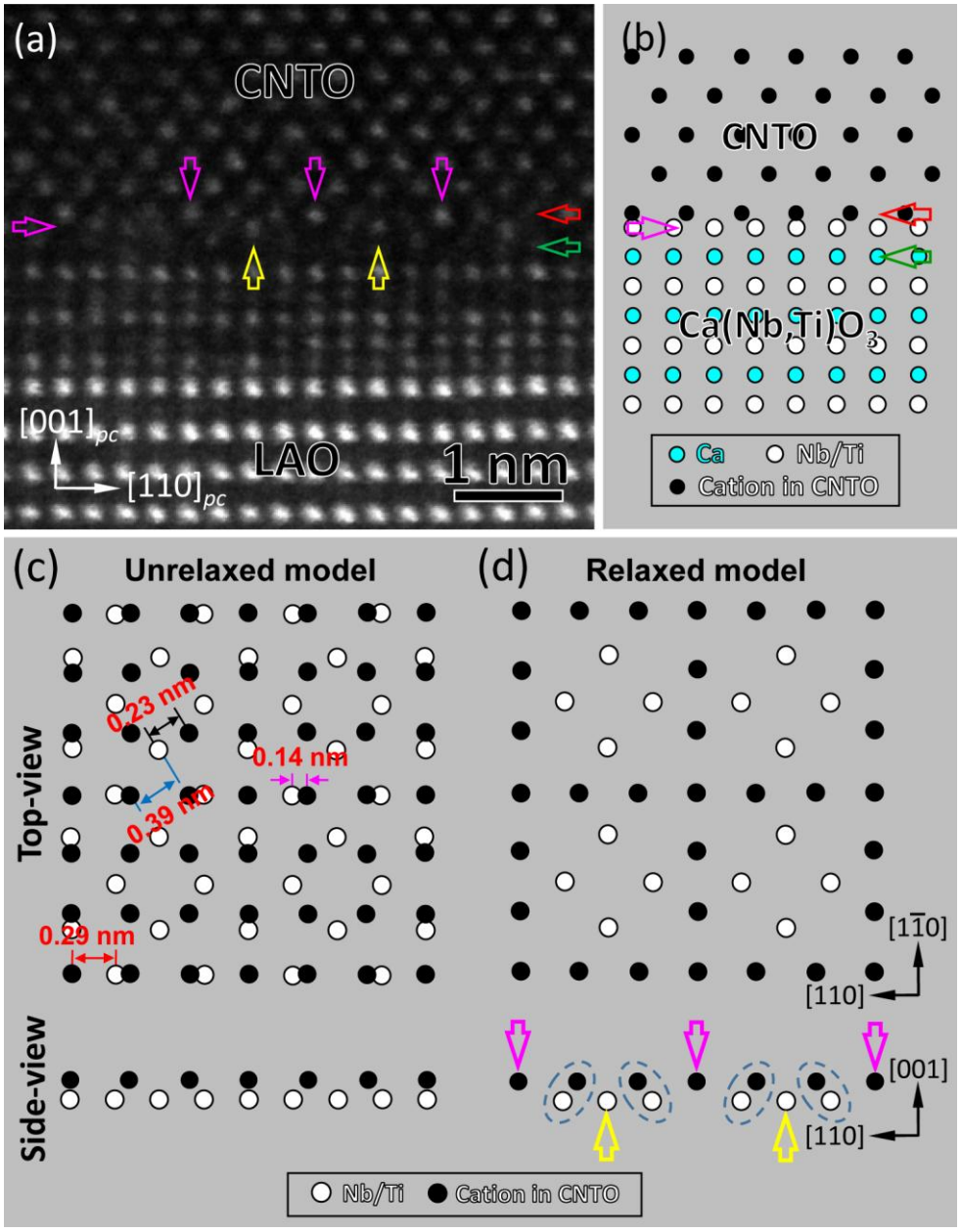
(a)
CNTO
LAO
1 nm
[001]pc
[110]pc
(b)
CNTO
Ca(Nb,Ti)O3
Ca
Nb/Ti
Cation in CNTO
(c)
Unrelaxed model
(d)
Relaxed model
Top-view
Side-view
0.23 nm
0.14 nm
0.39 nm
0.29 nm
[1$\bar{1}$0]
[110]
[001]
[110]
Nb/Ti
Cation in CNTO

FIG 5

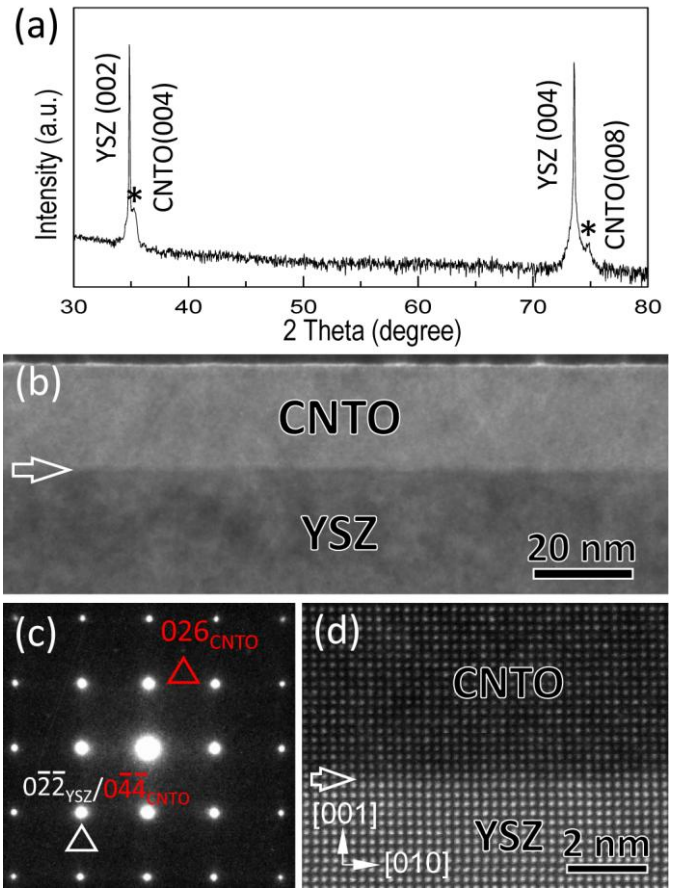
(a)
Intensity (a.u.)
YSZ (002)
CNTO(004)
YSZ (004)
CNTO(008)
30
40
50
60
70
80
2 Theta (degree)
(b)
CNTO
YSZ
20 nm
(c)
026CNTO
022YSZ/044CNTO
(d)
CNTO
[001]
[010]
YSZ
2 nm

FIG 6

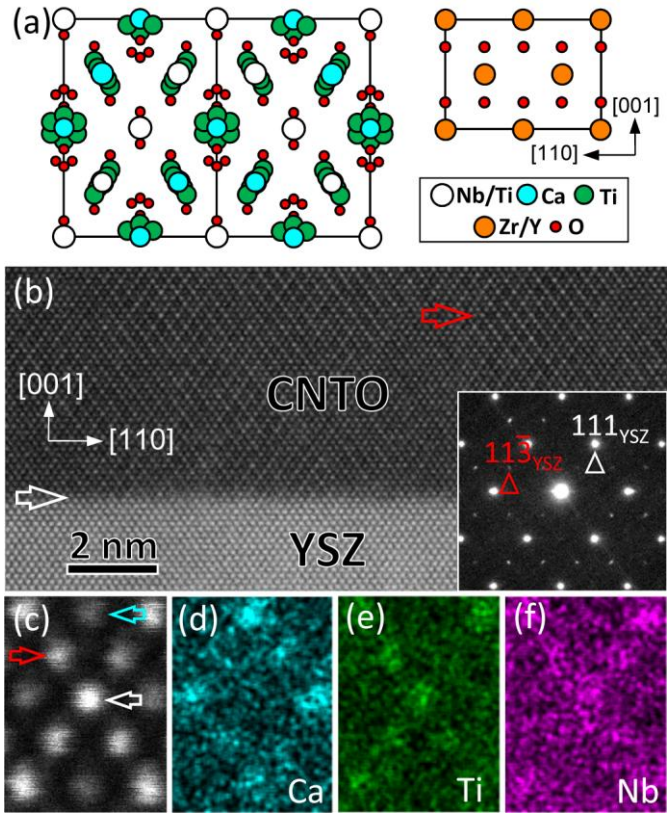
(a)
[001]
[110]
Nb/Ti
Ca
Ti
Zr/Y
O
(b)
[001]
[110]
CNTO
2 nm
YSZ
111YSZ
113YSZ
(c)
(d)
Ca
(e)
Ti
(f)
Nb